1 **A modelling study on the hydrodynamics of a coastal embayment occupied by**

2 **mussel farms (ría de Ares-Betanzos, NW Iberian Peninsula)**

3 Pedro Duarte[1*], Xosé Antón Alvarez-Salgado[2], Maria José Fernández-Reiriz[2], Silvia

4 Piedracoba[3], Uxio Labarta[2]

5

6 [1] Norwegian Polar Institute, N-9296 Tromsø, Norway (Pedro.Duarte@npolar.no)

7 [2] CSIC Instituto de Investigaciones Marinas, Eduardo Cabello 6, 36208 Vigo, Spain

8 [3] Universidad de Vigo, Departamento de Física Aplicada, Campus Lagoas-Marcosende,

9 36200 Vigo, Spain

10 * - Author for correspondence

11

12 **Key points**

13 • A 3-D hydrodynamic model was implemented for a Galician ría

14 • The importance of different hydrodynamic forcing functions was studied

15 • The impact of mussel cultivation rafts on circulation was analyzed

16

17 **Abstract**

18 The Ría de Ares-Betanzos is a partially stratified estuary in the NW Iberian upwelling

19 system where blue mussels are extensively cultured on hanging ropes. This type of

20 culture depends to a large extend on water circulation and residence times, since

21 mussels feed on suspended particles. Therefore, understanding the role of tides,

22 continental runoff, and winds on the circulation of this embayment has important

23 practical applications. Furthermore, previous works have stressed the potential

24 importance of aquaculture leases on water circulation within coastal ecosystems, with

25 potential negative feedbacks on production carrying capacity. Here we implemented and

26 validated a 3D hydrodynamic numerical model for the Ría de Ares-Betanzos to (i)

27 evaluate the relative importance of the forcing agents on the circulation within the ría

28 and (ii) estimate the importance of culture leases on circulation patterns at the scale of

29 the mussel farms from model simulations. The model was successfully validated with

30 empirical current velocity data collected during July and October 2007 using an

31 assortment of efficiency criteria. Model simulations were carried out to isolate the

32 effects of wind and river flows on circulation patterns. Model outputs suggest that (i)

33 both under upwelling and downwelling winds, the residual circulation keeps positive

34 with a strong influence from river discharge and a positive feedback from wind; and (ii)

35 mussel cultivation areas may reduce residual velocities by as much as 35%, suggesting

36 their potential feedbacks on food replenishment for cultivated mussels.

39

1   Introduction

The Galician rías are flooded tectonic valleys on the northwest coast of the Iberian Peninsula (Fig. 1). They are the ground for 40% of the European and 15% of the World production of blue mussels, about 250×10^6 kg year^{-1} [*Labarta et al*, 2004]. The cultivation system consist on hanging ropes (maximum length, 12 m) mounted on floating rafts (maximum size, 500 m^2) [*Pérez Camacho et al.*, 1991] of which there are over three and a half thousand in the five rías where these structures are installed [*Figueiras et al.*, 2002].

The large economic importance of these embayments, not only for mussel production but also for harbor, fishing, touristic and conservation activities, stimulated a large number of field studies on their physical, geochemical and biological features. Conversely, numerical modeling studies are scarce and focused mostly on circulation issues [*Torres–López et al*., 2001; *Souto et al*., 2003; *Carballo et al*., 2009]. Figueiras et al. (2002) reviewed some of the most important characteristics of these ecosystems justifying their high productivity. The subtidal circulation of the four Rías Baixas, to the south of Cape Fisterra (Fig. 1), is conditioned by the seasonal and short-term succession of upwelling and downwelling events on the adjacent shelf. The upwelling- favorable season starts between March and May and ends around early October [*Alvarez-Salgado et al*., 2000]. The upwelling-favorable season is characterized by the prevalence of northerly winds, with the Ekman pumping producing an inflow of upwelled water at the bottom of these embayments and a compensating outflow of surface waters (positive residual circulation). During the downwelling-favorable season, southerly winds prevail, provoking a reversal of this circulation pattern: Ekman pumping forces the

3

64 entry of shelf surface water into the embayment and a compensating outflow through

65 the bottom layer [*Piedracoba et al.*, 2005a].

66 The Ría de Ares-Betanzos, to the north of Cape Fisterra (Fig. 1), is 4–7 times smaller

67 than the Rías Baixas and oriented differently. As a consequence, Ekman pumping on the

68 adjacent shelf has a lower impact on the subtidal circulation of this embayment and

69 continental runoff gains more importance compared with the Rías Baixas [*Álvarez-*

70 *Salgado et al.*, 2011]. The Ría de Ares-Betanzos supports the production of 147 mussel

71 rafts, mostly concentrated along its southern margin (Fig. 1). This type of culture

72 depends to a large extend on water circulation and residence times, since mussel feed on

73 suspended living and non-living particles transported by water [*Navarro et al.*, 1991;

74 *Pérez-Camacho et al.*, 1995]. Previous works have stressed the potential importance of

75 aquaculture leases on water circulation within coastal ecosystems with potential

76 negative feedbacks on production carrying capacity [*Grant et al.*, 1998; *Grant and*

77 *Bacher*, 2001]. Following *Shi et al.* [2011], suspended aquaculture leases in Sungo Bay

78 (China) may cause a reduction on the average speed of surface current by 40%,

79 decreasing the exchange of water with the adjacent sea. Current speed reductions may

80 have important feedbacks on bivalve production and exploitation since they have

81 implications on the dispersal of mussel larvae before settlement [*Peteiro et al.*, 2011],

82 the availability of suspended food and the occurrence of harmful microalgae, which

83 limits the extraction of this resource [*Álvarez-Salgado et al.* 2008, 2011]. Therefore,

84 understanding the hydrodynamics of the Ría de Ares-Betanzos and the feedbacks from

85 cultivation leases on water circulation has important practical applications for the

86 sustainable management of this important culture.

87 Previous studies in the Ría de Ares-Betanzos have focused on phytoplankton diversity

88 and productivity [*Blanco*, 1985; *Mariño et al.*, 1985; *Bode and Varela*, 1998], nutrient

89 distributions [*Prego et al*., 1999], the physico-chemical structure of the benthic

90 environment [*Sánchez-Mata et al*., 1999] or the relationship between subtidal

91 circulation and net ecosystem metabolism [*Villegas-Ríos et al*., 2011]. The latter authors

92 implemented a 2-D transient box model to integrate physical, chemical and biological

93 data and to estimate fluxes between the inner and outer parts of the ría. They concluded

94 that, compared with the Rías Baixas, the subtidal circulation of the Ría de Ares-

95 Betanzos is positive both under upwelling and downwelling conditions as a result of the

96 larger relative importance of river flows [*Villegas-Rios et al*., 2011].

97 In this work, a 3D hydrodynamic model of the Ría de Ares-Betanzos was implemented

98 and validated and, thereafter, used to: (i) evaluate the relative importance of local winds,

99 tidal and river forcing processes on the circulation, providing a further test to the

100 explanations advanced by *Villegas-Ríos et al*. [2011] for the persistent positive residual

101 circulation; and (ii) access the importance of culture leases on residual circulation.

102 **2   Methods**
103

104 **2.1   Study site**
105

106 The Ría de Ares-Betanzos is the largest of six bays located between Cape Fisterra and

107 Cape Prior, in the NW coast of the Iberian Peninsula (Fig. 1), with a surface area of 72

108 km^2, a volume of 0.75 km^3 and a length of 19 km. It consists of two branches: Ares, the

109 estuary of river Eume and Betanzos, the estuary of river Mandeo with long-term

110 average flows of 16.5 and 14.1 m^{3}s^{-1}, respectively [*Prego et al*., 1999; *Sánchez-Mata et*

111 *al*., 1999]. The two branches converge into a zone that is freely connected to the

112 adjacent shelf through a mouth that is 40 m deep and 4 km wide.

2.2   Available data

Field data used in this work is described in *Villegas-Ríos et al.* [2011] and it was obtained in July and October-November of 2007. An acoustic Doppler (ACDP) current profiler was moored at stn 3 (Fig. 1) and covered the periods from 3 to 26 July and from 15 October to 20 November. Furthermore, continuous vertical profiles of salinity and temperature were recorded at stns A1, A2, B1, B2, 4 and 5 in the periods 9–23 July and 10–29 October (stn 5 was sampled only in October). These data was used for model initialization and validation.

Data on air temperature, relative humidity and light intensity from the meteorological station of Ferrol (Fig. 1) were downloaded from the web side of the Galician Weather Forecast Agency Meteogalicia (http://www.meteogalicia.es). Flows from rivers Eume and Mandeo were obtained as described in *Villegas-Ríos et al.* [2011]. Wind velocity and direction as well as river flows for the two periods under study are depicted in Fig. 2. Tide harmonics for A Coruña were obtained in *SHOM* [1984]. These data was used for model forcing (see below).

2.3   Hydrodynamic model

The model is based on the horizontal equations of motion (1 and 2), the equation of continuity (3 and 4), the equation of transport (5) and the hydrostatic and the Bousinesq assumptions [*Pond and Pickard*, 1983]:

$$\frac{\partial u_x}{dt} + \frac{\partial\ uu}{\partial x} + \frac{\partial\ uv}{\partial y} + \frac{\partial\ uw}{\partial z} - \nu_x \frac{\partial^2 u}{\partial_x 2} - \nu_y \frac{\partial^2 u}{\partial_y 2} - \nu_z \frac{\partial^2 u}{\partial_z 2} = -\frac{\partial P}{\rho \partial x} - \frac{Cf\,|u|u}{H} - \frac{Cd\,|u|udl}{2V} + \frac{\partial \tau_x}{\rho \partial z} + f v_y$$

(1)

$$\frac{\partial v\,y}{dt} + \frac{\partial\,vv}{\partial y} + \frac{\partial\,vu}{\partial x} + \frac{\partial\,vw}{\partial z} - v_x\frac{\partial^2 v}{\partial x^2} - v_y\frac{\partial^2 v}{\partial y^2} - v_z\frac{\partial^2 v}{\partial z^2} = -\frac{\partial P}{\rho\partial y} - \frac{Cf\,|v|\,v}{H} - \frac{Cd\,|v|\,vdl}{2V} + \frac{\partial \tau\,y}{\rho\partial z} - f u_x$$

(2)

$$\frac{d\xi}{dt} = \frac{\partial u\,x}{\partial x} + \frac{\partial v\,y}{\partial y} + \frac{\partial w\,z}{\partial z} \qquad (3)$$

$$\frac{\partial u\,x}{\partial x} + \frac{\partial v\,y}{\partial y} + \frac{\partial w\,z}{\partial z} = 0 \qquad (4)$$

$$\frac{\partial S}{dt} + \frac{\partial\,uS}{\partial x} + \frac{\partial\,vS}{\partial y} + \frac{\partial\,wS}{\partial z} = \frac{\partial\left(A_x\frac{\partial S}{\partial x}\right)}{\partial x} + \frac{\partial\left(A_y\frac{\partial S}{\partial y}\right)}{\partial y} + \frac{\partial\left(A_z\frac{\partial S}{\partial z}\right)}{\partial z} \qquad (5)$$

Where, u, v and w are the components of the current velocity (West-East (x), South-North (y) and Bottom-Up (z), respectively) (in m s^{-1}); P is the hydrostatic pressure (in N m^{-2}); ρ is the seawater density (in kg m^{-3}); v is the eddy diffusivity (East-West (x), North- South (y) and Bottom-Up (z), respectively) (in m^2 s^{-1}); Cf is the rugosity coefficient (dimensionless); Cd is the body drag coefficient (dimensionless); d and l are the width and height of the body against which drag is calculated (in m); τ is the wind stress (in N m^{-2}); f is the Coriolis parameter (in s^{-1}); ξ is the surface elevation/ water level (in m); H is the water depth (in m); S is the concentration of any dissolved or particulate property (in kg m^{-3}); and A is the diffusivity of the mentioned property along each of the three dimensions (in m^2 s^{-1}).

154   Equation 3 is applied at the surface, where flow divergence/convergence may change

155   surface elevation. Equation 4 is applied below the surface, where the balance of inflows

156   and outflows at any control volume must be zero.

157   The generic algorithm is:

158

159    $v_{ijk}^{t+1} \rightarrow \xi_{ij}^{t+\frac{1}{2}} \rightarrow u_{ijk}^{t+1} \rightarrow w_{ijk}^{t+1} \rightarrow V_{ijk}^{t+1} and \, \xi_{ij}^{t+1} \rightarrow S_{ij}^{t+1}$

160

161   The resolution is semi-implicit following an Alternate Direction Implicit (ADI) scheme.

162   Equations 1 and 2 are used to replace the velocity terms in the equation of continuity

163   (3). One of the velocity terms is explicit and the other is implicit. Equation 3 is

164   integrated vertically to estimate surface elevation implicitly ($\xi_{ijk}^{t+1/2}$), without the need to

165   know vertical velocities at this time and with vertical diffusivities cancelling each other

166   out. Obtained elevations at t+1/2 (half time step) are used in the pressure term of

167   equations 1 and 2, to calculate horizontal velocities (again, one of the velocity

168   components is calculated explicitly and the other is calculated implicitly). The pressure

169   term has a barotropic parcel that results from differences in water elevation and a

170   baroclinic parcel that results from water density differences. Afterwards, vertical

171   velocities are calculated with the continuity equation from the bottom till the surface. At

172   the surface layer, the numerical solution of equation 3 is used to obtain a final estimate

173   for the water level (ξ_{ijk}^{t+1}). Calculated velocities are then used in the transport equation to

174   calculate the concentration of dissolved or particulate substances (5).

175   In this model there are two drag terms: the first drag term in both equations 6 and 7 is

176   bottom drag (computed implicitly for stability) whereas the second drag term results

177   from drag exerted by a body within the water (for example: aquaculture leases). The

178   former term is computed only for bottom cells, whereas the latter is computed for cells

179   where mussel rafts are located. This drag is calculated as described in Morrison et al.

180   (1950):

181

182    $$D = \frac{1}{2}\rho.u^2.Cd.d.l \qquad (6)$$

183

184   Where, *Cd d* and *l* were defined above.

185   To get a force per unit of mass (acceleration), similar to the other parcels of both

186   equations, it is necessary to divide this equation by the mass of the water contained in a

187   certain volume, obtaining:

188

189    $$D = \frac{1}{2}\frac{Cd.u^2.\rho.d.l}{\rho V} \Leftrightarrow \frac{Cd.u^2.d.l}{2V} \qquad (7)$$

190

191   The implementation of this drag term was necessary to take into account the drag effects

192   of the hanging ropes from mussel rafts. Each raft has approximately 500 ropes

193   descending to a depth of up to 12 m. Each rope has a diameter of up to 12 cm, when

194   loaded with mussels. *Cd* may have values between 1 and 2 for flows approaching a

195   cylinder [*Fernandes et al*., unpublished]. Additionally, the effect of the ropes has to be

196   adjusted to the grid resolution of the model, i.e. defining the ropes density per horizontal

197   grid cell.

198   In this model, flows are solved at the sides of the grid cells, whereas surface elevations

199   and concentrations are calculated at the cells center. Horizontal advection terms are

200   calculated using an upwind scheme, whereas diffusion terms are based on a central

201   differences scheme. Vertical advection is computed with the Lax-Wendorf Total

202   Variation Diminishing (TDV) advection scheme described in *James* [1996], to reduce

203   numerical diffusion and allow a better simulation of vertical stratification. Horizontal

204   diffusivities are used as a calibration parameter, whereas vertical diffusivities are

205   computed with a mixing length model following *Nihoul* [1982] and *Santos* [1995].

206   The model is forced by tidal height at the sea boundaries, local winds and fresh water

207   flows. It includes a wet-drying scheme for intertidal areas, which consists of stop using

208   the advection term when depth is lower than a threshold value to avoid numerical

209   instabilities. Below this threshold the model computes all remaining terms – pressure,

210   bottom drag and Coriolis – while water depth is larger than 0.05 m. When this limit is

211   reached, computations do not take place in a given cell until a neighbor cell has a higher

212   water level, allowing then the pressure term to start 'filling' the 'dry' cell. Furthermore,

213   the model may add and remove surface layers during the simulation: if water depth of

214   the surface layer becomes smaller than a predefined threshold, this layer is added to the

215   second one. When the depth of this second layer becomes large enough is it divided in

216   two and the former surface layer is restored. This way it is possible to maintain a high

217   resolution near the surface without numerical problems arising when depth becomes too

218   small.

219 The model was implemented with EcoDynamo [*Pereira et al.*, 2006], an object-oriented

220 modeling software written in C++. There are different objects to simulate

221 hydrodynamic, thermodynamic and biogeochemical processes and variables. The shell

222 interface allows the user to choose among different models and to define the respective

223 setups – time steps, output formats (file, graphic and tables), objects to be used and

224 variables to be visualized. The list of objects, variables and parameters of model

225 equations are stored in specific files. Objects may communicate among them for data

226 exchange. In the present work the following objects were used: (i) Tide object, to

227 simulate water level at the sea boundaries, using harmonics for A Coruña (cf. –

228 Methodology – Available data); (ii) Air temperature object, storing air temperature data;

229 (iii) Wind object, storing wind velocities and directions; (iv) Light object, storing solar

230 radiation data; (v) Water temperature object, for water temperature calculation

231 following the equations described in *Portela and Neves* [1994]; (vi) Three-dimensional

232 hydrodynamic object, to solve the hydrodynamic equations mentioned above. The first

233 four objects act as forcing functions for both water temperature and hydrodynamic

234 calculations.

235 The horizontal spatial resolution of the model grid used in this work is 150 m, the

236 vertical resolution is between less than 1 m at the surface and up to c.a. 15 m at the

237 bottom layer corresponding to 107 lines x 121 columns x 15 vertical layers. Fig. 1

238 depicts a GIS image showing a chart of Ría de Ares-Betanzos, the location of sampling

239 stations used for model initialization and validation and a white line with the limits of

240 the model domain. A detail on the bathymetry used in the model is also shown.

241

242

2.3.1 Simulations

Simulations were run for 9–31 July and for 15 October–20 November 2007 for comparison with field data and also with residual flow estimates obtained by *Villegas-Ríos et al.* [2011] with a transient 2-D kinematic box model. Two simulations, hereafter named as "standard" were used for model validation. These simulations were forced with available meteorological data for the study period to be as realistic as possible. Afterwards, simulations were run without river flows or without wind or with a wind blowing always from the north or always from the south. Furthermore, simulations were run without taking into account the body drag exerted by the hanging ropes of mussel rafts. In all cases, only one condition was tested at each time. Comparing standard simulations with those without river flows allows estimating the relative importance of continental runoff in establishing the positive residual circulation pattern. Comparing standard simulations with those without wind and with those with a wind oriented in the North-South direction allows understanding the relative importance of local wind forcing on the observed residual circulation. Finally, comparing standard simulations with those without mussel rafts body drag allows estimating the effect of the mussel farms on the circulation of the ría. Table 1 synthesizes the set of simulations carried out in this study and corresponding abbreviations.

Validation

For the purposes of model validation, field data collected in July and October 2007 were used to compare with July and October standard simulations (see above and Table 1). Current velocity time series obtained at stn 3 (Fig. 1) were compared with model results. A correspondence had to be established between water layers monitored by the ACDP current meter and model layers. Accordingly, model predicted velocities were

268 averaged for layers: (i) 1 till 5 for comparison with current meter surface layer data; 6 to

269 8, for comparison with current meter intermediate layer data; (iii) 9 to 12, for

270 comparison with current meter deeper layer data. Furthermore, vertical temperature and

271 salinity profiles available for the same periods were also compared with those obtained

272 with the model. However, since there was no available salinity and water temperature

273 data along the sea boundary for the simulation period, it was not possible to do a

274 realistic simulation for these variables. Therefore, available data for the outermost

275 station (stn 4, refer Fig. 1) at the starting simulation dates were assumed for the whole

276 simulation period.

277 The overall correspondence between data records and simulated values was analyzed

278 using Model II linear regression analysis, as suggested by *Laws and Archie* [1981], with

279 the major axis regression method as recommended by *Mesplé et al*. [1996] and

280 described in *Sokal and Rohlf* [1995]. ANOVA was used to test the variance explained

281 by the model. Furthermore, several efficiency criteria were used: the root mean square

282 error (RMSE), the Nash-Sutcliffe efficiency (E) [*Nash and Sutcliffe*, 1970], the index of

283 agreement (d) [*Wilmott*, 1981], their modified versions E1 [*Wilmott*, 1981] and d1

284 [*Krause et al*., 2005], respectively, and the cost function (CF) (OSPAR commission,

285 1998). Whenever available in the literature, qualitative criteria were adopted (Table 2).

286 **3   Results**

287 **3.1   Model performance**
288

289 Predicted and observed *u* and *v* velocity components at stn 3 for the standard October

290 simulation are shown in Fig. 3 for the intermediate layers. Model simulations fitted well

291 with the measured data for the intermediate and deeper layers but not for the surface

292 ones. Similar results were obtained for the July standard simulation (not shown). A

293 synthesis of model II linear regression analysis between empirical and simulated data

294 for both velocity components is presented in Table 3 together with the results obtained

295 for the assortment of efficiency criteria defined in the methods section. With the

296 exception of results obtained for the surface layers, the slopes of the regression lines

297 tend to be close to one and the y-intercepts tend to be close to zero. Deviations of the

298 former from one would suggest that differences between model predictions and

299 observations are proportional to variable values, whereas deviations of the latter from

300 zero indicate a bias that would affect model results equally for all values of the variables

301 being simulated. In spite of the poor fit between model and observed results at the

302 surface layer, with the simulations generally overestimating the current velocities, the

303 variance explained by the model was very large compared to the unexplained variance

304 ($p \ll 0.001$ for all simulations). RMSE was< 5 cm s^{-1} except in a few cases. Results

305 obtained with the various efficiency criteria suggest that the model behaved poorly for

306 the surface layers but the performance was generally good, very good or even excellent

307 for the intermediate and the deeper layers for, at least, two efficiency criteria. However,

308 concerning CF, all simulation results were good or very good, even for the surface

309 layers. The d and d1 criteria lack a quality scale, to the best of our knowledge. However,

310 considering that its values may range from zero to one (the best possible result) and that

311 all obtained values for the intermediate and deeper layers are equal or larger than 0.6,

312 model results seem, at least, reasonably good according to this index of agreement.

313 Observed and predicted (standard simulations) vertical profiles of water temperature

314 and salinity are shown in Fig. 4 for July 19th (stns 4, 3, A1 and B1). The water column

315 was thermally stratified in July with temperatures ranging from almost 20°C at the

316 surface to nearly 15°C at 25–30 m depth, both for observed and predicted results. There

14

317 was also haline stratification, with surface water values around 34.5 and deeper water

318 values (at c.a. 30 m) around 35.5. Surface salinities at inner stations A1 and B1, under

319 the direct influence of rivers Eume and Mandeo, respectively, were slightly lower than

320 values observed at the other stations. In what concerns October data (not shown),

321 considering both the observed and predicted results, the water column was well mixed

322 with a temperature difference between the surface and the deeper layers of less than

323 0.5^{o}C. Salinity was almost vertically homogeneous, with a maximal difference of c.a.

324 0.5 units in station A1.

325 **3.2   Standard residual circulation patterns**
326

327 Figs. 5 and 6 show residual velocities for the surface and bottom layers of the Ría de

328 Ares-Betanzos in July and October, respectively. These values were calculated from

329 predicted velocities integrated for the upper eight and for the lower seven layers.

330 Previously, we verified that residual velocities showed opposite directions in these two

331 sets of layers. Predicted residual circulation patterns are clearly positive in July, with a

332 marked water inflow below layer 8 (c.a. 10 m depth) and outflow at shallower depths.

333 The most remarkable feature of the simulated surface circulation of the ría in this period

334 (Fig. 5a & b) is the cyclonic gyre that develops in the confluence zone between the

335 estuaries of the rivers Eume and Mandeo, in the middle ría, which produces a weak

336 inflow of surface water through the southern side of the ría and strong outflow through

337 the northern side. It is also remarkable that the freshwater excess introduced by both

338 rivers preferentially leaves the ría through the northern side. This means that the outflow

339 of the River Mandeo should displace first north along the eastern side of the ría, meet

340 the River Eume flow and, then, both turn left to leave the ría. The simulated flow in the

341 bottom layer shows a marked divergence just below the cyclonic gyre of the surface

15

342 layer with part of the water entering the Eume and the other part the Mandeo estuary

343 (Fig. 5b). This divergence is the probable reason behind the surface cyclonic circulation.

344 Although less well-defined, a similar residual circulation pattern was produced by the

345 standard October simulations (Fig. 6a & b).

346

347 Figures 7 and 8 depict the average residual flows (in m^3 s^{-1}) calculated with the current

348 velocities produced by the various simulations for the periods (16-23 July 2007 and 15-

349 28 October 2007) and the boundaries covered by the inverse 2D box model of *Villegas-*

350 *Ríos et al*. [2011]. Earlier dates were not used for comparisons to allow an initial model

351 spin-up of, at least, five days. Those boundaries were chosen for the sake of comparison

352 of the results of the numerical and the inverse models and to get a simplified picture of

353 the 2-layer residual circulation of the embayment. Flows calculated for the July standard

354 simulation (Fig. 7a) were higher than those for the October standard simulation (Fig.

355 7b). The magnitude of the flows was larger at the boundary located on the sea side with

356 some values above 200 m^3 s^{-1}. Residual flows across the inner boundaries are much

357 lower than those predicted for the outer boundary, with the lowest values for the inner

358 northern boundary.

359 **3.3 Effect of continental runoff and local winds on the residual circulation**
360 **pattern**
361 Removing river flows has a large decreasing effect on residual flows in July (up to 50%

362 reduction; Fig. 7c), but not in October (Fig. 7d). Removal of the local wind forcing has

363 a strong effect both in July (Fig. 8a) and October (Fig. 8b). In July, the effect was

364 stronger than the removal of river flows. Forcing the model with northerly winds would

365 have almost no effect in July but an important effect in October (Fig. 8c & d), with an

366 increase in the residual flows at the northern inner boundary by almost 100% in

367 comparison with the standard simulation. Regarding the results obtained with southerly

368   wind forcing, there was an important increase in residual circulation across the outer

369   boundary both in July (Fig. 8e) and October (Fig. 8f). In the case of the latter, there was

370   also a remarkable decrease in the residual circulation across the inner northern boundary

371   associated with a change in the direction of the surface flow.

372   **3.4   Effect of mussel farms on the residual circulation pattern**
373

374   The percentage of reduction in residual velocities (Fig. 9), calculated from the

375   differences between the simulation without mussel farms and the standard simulation,

376   for the study period in July, suggests that body drag exerted by the mussel rafts may

377   lead to a slowness of the residual currents of almost 40%.

378   **4   Discussion**
379

380   The model reproduced reasonably well the velocity field at the intermediate and bottom

381   layers. However, despite the good results obtained with some validation criteria, such as

382   the cost function, the agreement between measured and modeled currents was not so

383   satisfactory for the surface layer. Such a disagreement cannot be imputed exclusively to

384   the performance of the model. It is well known that the ability of the DCM12 to

385   measure the current in the surface layer is negatively affected in such a way that the

386   most energetic tidal harmonics were not found in the surface layer (1–5 m), as could be

387   expected, but in the second one [*Míguez*, 2003; *Piedracoba et al*. 2005a]. Whether this

388   is a natural physical process (wind/wave induced turbulence at the surface layer) or an

389   instrumental artifact is not clear yet. Because the DCM12 was designed to reduce the

390   side-lobe effect [*Aanderaa et al*. 1995, *Aanderaa Instruments*, 1999], this can cause

391   artificial effects on surface measurements that lead to under estimate of surface

392   velocities [*van Haren*, 2001]. It is also remarkable that the vertical stratification is

393   reasonably well reproduced by the model both for temperature and salinity.

394   Exchange flows calculated by *Villegas-Rios et al.* [2011] across the three boundaries

395   defined in Figure 7 with a 2-D kinematic box model were significantly higher that the

396   outputs of the standard simulations. Although a 2-D positive residual circulation pattern

397   was shown by both the inverse and the numerical model, the values of the former were

398   from twofold (in July) to tenfold (in October) larger that the latter. It should be noted

399   that the 2-D box model of *Villegas-Ríos et al.* [2011] was based on the integration of

400   simplified versions of the equations of continuity (4) and salinity conservation (5):

401

402    $$\overline{Q}_S = \overline{Q}_B + \overline{Q}_R + \overline{P} - \overline{E} \tag{8}$$

403

404    $$V \frac{\Delta S}{\Delta t} = \overline{Q}_B \overline{S}_B - \overline{Q}_S \overline{S}_S \tag{9}$$

405

406   Where $\overline{Q}_B$, $\overline{Q}_S$, $\overline{Q}_R$, $\overline{P}$ and $\overline{E}$ (m^{3}s^{-1}) are, respectively, the horizontal bottom and surface

407   subtidal flows at the open boundary of each of the 3 boxes defined in Figs, 7 and 8,

408   continental runoff, precipitation and evaporation, between two consecutive surveys.

409    $\overline{S}_S$ and $\overline{S}_B$ (kg m^{-3}) are the salinities at the bottom and surface layers of each boundary,

410   averaged over two consecutive surveys. To obtain $\overline{S}_S$ and $\overline{S}_B$, they used the salinity

411   profiles collected on each survey and assumed that this salinity was representative for

412   the whole cross section that defines the boundary of each box. This is equivalent to

413   assume that the water flow is homogeneous throughout each cross section. However,

414   the standard model simulations (Fig. 5 & 6) predicts a marked lateral gradient in the

415   residual circulation, mainly in the middle ría, where the predicted flows through the

416   northern side of the embayment are an order of magnitude stronger than through the

417   southern side. Furthermore, there are cases where there is an inflow of surface water

418   through the southern side resulting in the cyclonic gyre previously described.

419   Considering that   and   were negligible during both study periods [*Villegas-Ríos et*

420   *al.*, 2011] 8 may be simplified to:

421

422    $$\overline{Q_S} = \overline{Q_B} + \overline{Q_R}$$ (10)

423

424   Inserting 10 into 9 and solving for   :

425

426    $$\overline{Q_B} = \frac{V\frac{\Delta S}{\Delta t} + \overline{\overline{Q_R S_S}}}{S_B - \overline{S_S}}$$ (11)

427

428   Equation 11 implies that very small differences in bottom and surface salinities will lead

429   to very high bottom flow estimates and, consequently, to very high surface flow

430   estimates. Therefore, when water is weakly stratified, as in October 2007, higher flow

431   estimates are more likely to be obtained. Therefore, our guess is that the disagreement

432   between the results of the kinematic and the numerical model should be more due to the

assumptions made to run the kinematic model than to a failure of the numerical model
to reproduce the circulation pattern of the ría.

In support of the model results there are some indirect evidences: i) despite that almost
100% of the adult mussels are located in the mussel farms of the southern side of the
ría, the site where mussel seeds are collected more efficiently is, surprisingly, the
northern outer side of the ría *[Peteiro et al.*, 2011]. The surface circulation pattern
predicted by the model would explain this dislocation between the site of massive
gamete production and the site of massive larvae settlement; ii) despite the closeness of
the mussel farm area of Arnela to the mouth of the River Mandeo, surface salinities at
that site are not coupled to the Mandeo river flow [*Isabel et al.*, *in prep.*]. This is
consistent with the preferential displacement of the freshwater discharged by the River
Mandeo to the North, to meet the outflow of the river Eume suggested by the model
simulations; iii) If the current velocity profile in the central segment of the ria were
representative of the whole cross section, the renewal of this embayment would be from
two to tenfold faster than predicted by the model, which would be hardly compatible
with the observed warming of the surface layer and the recurrent closure of mussel
cultivation areas because of the occurrence of harmful microalgae characteristic of
highly stratified sites with very low flushing rates [*Álvarez-Salgado et al.*, 2011].

Concerning the modeled residual flows, differences between input and output values are
expected to be matched by river flows. However, when inputs and outputs are compared
in Figs. 7 and 8 there are situations when the former are larger than the latter. This is not
the result of some violation of the conservation law, but just the result of the net
changes in water height along the periods used to calculate residual flows. In fact, tests
conducted for longer periods when initial and final heights were similar confirmed that
the model is conservative.

458   The comparison of July 2007 simulations with and without river flows (cf. Table 1)

459   suggests the importance of the latter in the intensity of residual circulation during that

460   period. However, a similar comparison with the October 2007 simulations suggests the

461   opposite. This is an obvious consequence of the larger river flows in July 2007 (average

462    $= 5.7$ m^3 s^{-1}) compared with those of October 2007 (average $= 2.8$ m^3 s^{-1}) (c.f. – Fig. 2).

463   The comparison of July and October simulations with and without the wind effect

464   suggests the strong effect of the wind forcing, especially in the July simulation.

465   Therefore, it may be concluded that it is hard to generalize on the relative weight of

466   these two potentially important forcing mechanisms that will change as a function of

467   their respective magnitude. However, within the ranges covered by the present study

468   periods and model simulations it seems that local wind have the potential for a larger

469   effect on the intensity of input/output residual flows than the river outputs.

470   When the standard simulations are compared with those with a persistently meridional

471   wind (Figs. 5-8), model results suggest that southerly winds have a stronger effect on

472   residual circulation, increasing the intensity of the input/output flows across the outer

473   boundary. Again, the differences in the patterns obtained for July and October are a

474   result of the large differences in wind velocity for both periods. In the case of October,

475   northerly winds seem to have an effect of blockage of the residual circulation along the

476   outer boundary (Fig. 6): both surface and bottom residual velocities under persistent

477   northerly wind produce a strong south-westward current along the outer boundary of the

478   model, preventing the exchange between the ría and the adjacent shelf. However, it is

479   important to keep in mind that this effect could be merely an artifact resulting from the

480   close location of the sea boundary that prevents the integration of mesoscale effects on

481   model dynamics rather than a real phenomenon. Possibly, the orientation of this ría

482   implies an influence of meridional winds slightly different from that observed for the

21

483   Rías Baixas, that are perpendicular to the shore (Fig. 1). In Ares-Betanzos, a perfectly

484   meridional northerly wind would force the water towards the south-western margin,

485   possibly explaining the above mentioned blockage of the circulation. Such an effect

486   would not be observed with a perfectly meridional southerly wind because most of the

487   north-western boundary is open and, therefore, the model does not receive the feedback

488   of the interaction of water circulation with land boundaries.

489   The impact of mussel cultivation on hydrodynamics may correspond to large reductions

490   in residual current velocities (up to 40%) suggesting the potential for mussel rafts to

491   influence water flows and, therefore, water and food renewal for the cultivated species.

492   This is a potentially negative feedback to the cultivation process, in line with findings

493   by other authors. *Grant et al*. [1998] applied the methodology of drag calculation within

494   a kelp forest, described by *Jackson and Winant* [1983], to estimate drag exerted by

495   mussel rafts in Saldanha Bay (South Africa). *Grant and Bacher* [2001], working with a

496   two-dimensional vertically integrated finite element model to simulate current velocities

497   in Sungo Bay (China), used Manning coefficients of 0.03 and 0.15 for non-aquaculture

498   and aquaculture areas, respectively, to account for the slow down effects of aquaculture

499   structures on the flow. The same approach was followed by *Duarte et al.* [2003] for the

500   same ecosystem. *Shi et al*. [2011] estimated that body drag exerted by kelp cultivation

501   in Sungo Bay may cause a 40 % reduction in average speed of surface current, using a

502   similar approach to the one described in the present study. *Delaux et al*. [2011] used 2D

503   high resolution computational fluid dynamics model to investigate the influence of

504   block spacing and angle in suspended shellfish long-line cultures and obtained flow

505   reductions of up to 25%.

5   Conclusions

In this work a 3D hydrodynamic model was implemented to Ría de Ares-Betanzos and validated with empirical data on current velocities and vertical salinity and temperature profiles. Results from model simulations suggest the existence of a cyclonic gyre that develops in the confluence zone between the estuaries of the rivers Eume and Mandeo, in the middle ría, consistent with empirical evidence on mussel larval dispersion. Furthermore, residual circulation seems to be always positive with a bottom inflow and a surface outflow, irrespective of local wind regime and as a probable result of river flows and the geographic orientation of this system, unlike what has been observed in Rías Baixas to the south of Cape Fisterra. Substantial reduction of the subtidal circulation of the Ría de Ares-Betanzos has been predicted because of the presence of mussel farms, not only locally, but at the scale of the whole embayment. A reduction of the flow would affect negatively the carrying capacity of the mussel farms and would favor the occurrence of harmful microalgae that proliferates in stratified slow moving environments. On this light, and claiming the principle of precaution, a cornerstone of the sustainable exploitation of marine living resources, we suggest incorporating this kind of numerical models to the scientific advice of policymakers involved in the regulation of extensive aquaculture.

6   Acknowledgements

23

7 References

530 **7 References**

531

532 1. Aanderaa, I., Iversen, S. and S. Forbord (1995), Acoustic Doppler current

533   meter: shallow water harbor application, Sea Technology, 43.

534 2. Aanderaa Instruments (1999), Doppler Current Meter, DCM 12, Reliability and

535   comparison tests, in Sensor & Systems, A newsletter from Aanderaa

536   Instruments, Aanderaa Instruments, 4 pp.

537 3. Allen, J.I., Holt, J.T., Blackford, J. and R. Proctor (2007), Error quantification of

538   a high-resolution coupled hydrodynamic-ecosystem coastal-ocean model: Part 2.

539   Chlorophyll-a, nutrients and SPM, J. Marine Syst., 68 (3-4), 381-404, doi:

540   10.1016/j.jmarsys.2007.01.005.

541 4. Álvarez Salgado, X.A., Gago, J., Míguez, B.M., Gilcoto, M. and F.F. Pérez

542   (2000), Surface waters of the NW Iberian Margin: Upwelling on the shelf versus

543   outwelling of upwelled waters from the Rías Baixas, Estuar. Coast. Shelf S., 51

544   (6), 821-837, doi: 10.1006/ecss.2000.0714

545 5. Álvarez-Salgado, X.A., Figueiras, F.G., Fernández-Reiriz, M.J., Labarta, U.,

546   Peteiro, L. and S. Piedracoba (2011), Control of lipophilic shellfish poisoning

547   outbreaks by seasonal upwelling and continental runoff, Harmful Algae, 10 (2),

548   121–129, doi:10.1016/j.hal.2010.08.003.

549 6. Blanco, J. (1985), Algunas características del fitoplâncton de Lorbé (ría de Ares

550   y Betanzos) en primavera, Bol.Inst.Esp.Oceanogr., 2 (2), 17–26.

551 7. Bode, A. and M. Varela (1998), Primary production and phytoplankton in three

552   Galician Rias Altas (NW Spain): seasonal and spatial variability, Sci. Mar., 62

553   (4), 319–330.

554   8. Carballo, R., Iglesias, G. and A. Castro (2009), Residual circulation in the ría de

555   Muros (NW Spain): A 3D numerical model study, J. Marine Syst., 75 (1-2),

556   116–130, doi: 10.1016/j.jmarsys.2008.08.004.

557   9. Delaux, S, Stevens, C.L. and S. Popinet, (2011), High-resolution computational

558   fluid dynamics modeling of suspended shellfish structures, Environ. Fluid.

559   Mech., 11 (4), 405–425, doi: 10.1007/s10652-010-9183.

560   10. Duarte, P., Meneses, R., Hawkins, A.J.S., Zhu, M., Fang, J. and J. Grant (2003),

561   Mathematical modelling to assess the carrying capacity for multi-species culture

562   within coastal waters, Ecol. Model., 168, 109-143,

563   doi:10.1016/j.ecolmodel.2005.05.012.

564   11. Fernandes, L., Saraiva, S., Leitão, P.C., Pina, P., Santos, A., Braunschweig, F.,

565   and R. Neves, R. (2008), Code, tests and presentation of results of small scale

566   applications relevant for field campaign data; parameterisations of modules – 3D

567   model of a mussel raft. Managing benthic ecosystems in relation to physical

568   forcing and environmental constraints (MaBenE), EVK3-2001-00144.

569   12. Figueiras, F.G., Labarta, U. and M.J. Fernández-Reiriz (2002), Coastal

570   upwelling, primary production and mussel growth in the ría Baixas of Galicia,

571   Hydrobiologia, 484 (1-3), 121–131, doi: 10.1023/A:1021309222459.

572   13. Grant, J., S.D., J., Monteiro, P., Pitcher, G. and K. Heasman (1998), Shellfish

573   culture in the Benguela system: a carbon budget of Saldanha Bay for raft culture

574   of *Mytilus galloprovincialis*, J. Shellfish Res., 17 (1-3), 41–49.

575   14. Grant, J. and C. Bacher (2001), A numerical model of flow modification induced

576   by suspended aquaculture in a Chinese Bay. Can. J. Fish. Aquat. Sci., 58, 1–9.

577   15. James, I.D. (1996) Advection schemes for shelf sea models. J. Marine Syst., 8

578   (3), 237-254.

579   16. Jackson, G.A. and C.D. Winant (1983), Effect of a kelp forest on coastal
580   currents, Cont. Shelf Res., 2 (1), 75–80.

581   17. Krause, P., Boyle, D.P. and F. Bäse (2005), Comparison of different efficiency
582   criteria for hydrological model assessment, Advances in Geosciences, 5, 89-97,
583   doi: 10.5194/adgeo-5-89-2005.

584   18. Labarta, U., Fernández-Reiriz, M.J., Pérez-Camacho, A. and E. Pérez-Corbacho
585   (2004), Bateeiros, Mar, Mejillón. Una Perspectiva Bioeconómica (Serie Estudios
586   Sectoriales), Fundación CaixaGalicia, A Coruña, España.

587   19. Laws, E. A. and J.W. Archie (1981), Appropriate use of regression analysis in
588   marine biology, Mar. Biol., 65 (1), 99–118.

589   20. Maréchal, D. (2004), A soil-based approach to rainfall-runoff modelling in
590   ungauged catchments for England and Wales, PhD Thesis, Cranfield University.

591   21. Mariño, J., Campos, M., Nunes, M. and M. Iglesias (1985), Variación estacional
592   de los factores ambientales y del fitoplâncton en la zona de Lorbé (ría de Ares y
593   Betanzos) en 1978, Bol. Inst. Esp. Oceanogr., 2 (1), 88–99.

594   22. Mesplé, F., M. Trousselier, C. Casellas and P. Legendre (1996), Evaluation of
595   simple statistical criteria to qualify a simulation, Ecol. Model., 88, 9–18, doi:
596   10.1016/0304-3800(95)00033-X.

597   23. Míguez, B.M. (2003), Descripción dinámica de la circulación en dos Rías
598   Baixas: Vigo y Pontevedra, Ph.D. Thesis, Universidade de Vigo, Vigo, Spain.

599   24. Morrison, J.R., O'Brien, M.P., Johnson, J.W. and S.A. Schaaf (1950), The forces
600   exerted by surface waves on piles, Petroleum transactions, AIME, Vol. bold
601   189, 149-154.

602 25. Nash, J.E. and J.V. Sutcliffe (1970), River flow forecasting through conceptual

603   models. Part I – a discussion of principles, J. Hydrol., 10 (3), 282-290,

604   doi:10.1016/0022-1694(70)90255-6.

605 26. Navarro, E., Iglesias, J.I.P., Perez-Camacho, A., Labarta, U. and R. Beiras

606   (1991), The physiological energetics of mussels (*Mytilus galloprovincialis* Lmk)

607   from different cultivation rafts in the Ria de Arosa (Galicia, N.W. Spain),

608   Aquaculture, 94 (2-3), 197–212.

609 27. Nihoul, J.C.J. (1982), Oceanography of semi-enclosed seas. Hydrodynamics of

610   Semi-Enclosed Seas, J.C.J. Nihoul Ed., Elsevier Publ Co., Amsterdam, pp.1-12.

611 28. OSPAR Commission (1998), Report of the modeling workshop on

612   eutrophication issues. 5–8 November, Den Haag, The Netherlands, OSPAR

613   Report, 86 pp.

614 29. Pereira, A., Duarte, A. and A. Norro (2006), Different modelling tools of aquatic

615   ecosystems: A proposal for a unified approach, Ecological Informatics 1, 407-

616   421, doi:10.1016/j.ecoinf.2006.09.004.

617 30. Pérez-Camacho, A., González, R. and J. Fuentes (1991), Mussel culture in

618   Galicia (N.W. Spain), Aquaculture, 94, 263–278.

619 31. Pérez-Camacho, A., Labarta, U. and R. Beiras (1995), Growth of mussels

620   (*Mytilusedulis galloprovincialis*) on cultivation rafts: influence of seed source,

621   cultivation site and phytoplankton availability, Aquaculture, 138 (1-4), 349–362,

622   doi: 10.1016/0044-8486(95)01139-0.

623 32. Piedracoba, S., Álvarez Salgado, X.A., Rosón, G. and J.L. Herrera (2005a),

624   Short-timescale thermohaline variability and residual circulation in the central

625   segment of the coastal upwelling system of the Ríade Vigo (northwest Spain)

626   during four contrasting periods, J. Geophys. Res., 110 (C03018), 1 − 15,

627   doi:10.1029/2004JC002556.

628 33. Piedracoba, S., Souto, C., Gilcoto, M. and P.C. Pardo (2005b), Hydrography and

629   dynamics of the Ría de Ribadeo (NW Spain), a wave driven estuary. Estuar.

630   Coast. Shelf Sci., 65 (4), 726–738, doi: 10.1016/j.ecss.2005.07.013.

631 34. Pond, S. and G. Pickard (2003), Introductory dynamical oceanography, Elsevier

632   Butterworth-Heinemann, Oxford.

633 35. Portela, L.I. and R. Neves (1994), Modelling temperature distribution in the

634   shallow Tejo estuary, in Advances in Water Resources Technology and

635   Management, edited by Tsakiris and Santos, pp. 457–463, Balkema, Rotterdam.

636 36. Prego, R., Barciela, M.C. and M. Varela (1999), Nutrient dynamics in the

637   Galician coastal area (Northwestern Iberian Peninsula): do the Rias Bajas

638   receive more nutrient salts than the Rias Altas?, Cont. Shelf. Res., 19 (3), 317–

639   334, doi: 10.1016/S0278-4343(98)00099-5.

640 37. Radach, G. and A. Moll (2006), Review of three-dimensional ecological

641   modeling related to the North Sea shelf system. Part II: model validation and

642   data needs, Oceanogr. Oceanogr. Mar. Biol., An Annual Review, 44: 1-60, doi:

643   10.1201/9781420006391.ch1.

644 38. Sánchez-Mata, A., Glémarec, M. and J. Mora (1999), Physico-chemical

645   structure of the benthic environment of a Galician ría (ría de Ares-Betanzos,

646   north-west Spain). J. Mar. Biol. Ass. U.K., 79 (1): 1-21, doi: http://dx.doi.org/.

647 39. Santos, A. (1995), Modelo hidrodinâmico tridimensional de circulação oceânica

648   estuarina, PhD thesis, Universidade Técnica de Lisboa.

649 40. Shi, J., Wei, H., Zhao, L., Yuan, Y., Fang, J. and J. Zhang (2011), A physical–
650   biological coupled aquaculture model for a suspended aquaculture area of China,
651   Aquaculture, 318, 412–424, doi:10.1016/j.aquaculture.2011.05.048.

652 41. SHOM - Service Hydrographique et Océanographique de la Marine (1984),
653   Table des marées des grands ports du Monde. Service Hydrographique et
654   Océanographique de la Marine.

655 42. Sokal, R. R. and F. J. Rohlf (1995), Biometry. The Principles and Practice of
656   Statistics in Biological Research, WH. Freeman and Company.

657 43. Souto, C., Gilcoto, M., Fariña-Busto, L. and F.F. Pérez (2003), Modelling the
658   residual circulation of a coastal embayment affected by wind driven upwelling:
659   circulation of the ría de Vigo (NW Spain), J. Geophys. Res., 108 (C11): 3340–
660   3358, doi:10.1029/2002JC001512.

661 44. Torres-López, S., Varela, R.A. and E. Delhez (2001), Residual circulation and
662   thermocline distribution of the ría de Vigo: a 3-D hydrodynamical model. Sci.
663   Mar., 65, (Suppl. 1): 277–289.

664 45. van Haren, H. (2001), Estimates of sea level, waves and winds from a bottom-
665   mounted ADCP in a shelf sea. J. Sea Res., 45 (1), 1–14, doi: 10.1016/S1385-
666   1101(00)00060-5.

667 46. Villegas-Ríos, D., Álvarez-Salgado, Piedracoba, S., Rosón, G., Labarta, U. and
668   M.J. Fernández-Reiriz (2011), Net ecosystem metabolism of a coastal
669   embayment fertilised by upwelling and continental runoff. Cont. Shelf Res., 31:
670   400-413, doi:10.1016/j.csr.2010.07.010.

671 47. Wilmott, C.J., 1981. On the validation of models. Physical Geography 2 (2):
672   184-194.

673

674

675 **Tables**

676

677 Table 1 – Model simulations and corresponding abbreviations.

Period	Simulation	Abbreviation
July	Standard	July-St
	Without rivers	July-1
	Without wind	July-2
	With northerly wind	July-3
	With southerly wind	July-4
	Without body drag due to the mussel rafts	July-5
October	Standard	October-St
	Without rivers	October-1
	Without wind	October-2
	With northerly wind	October-3
	With southerly wind	October-4

678

679

680 Table 2 – Measures of reliability synthesized in *Allen et al*. [2007].

	Excellent	Very good	Good	Poor
Nash Sutcliffe model efficiency (**E**) [*Nash and Sutcliffe*, 1970] and *Maréchal* [2004] for quality level criteria	> 0.65	0.65-0.5	0.5-0.2	< 0.2

	Very good	Good	Reasonable	Poor
Cost function (**CF**) [*OSPAR Commission*, 1998]	≤ 1	1-2	2-5	≥ 5
Cost function with quality criteria according to *Radach and Moll* [2006]			2-3	≥ 3

681

682

683

684

685

686 Table 3 – Model validation. For each of the two standard simulations (cf. – Methodology) and for each velocity component (west-east (u) and
687 south-north (v)) parameters of the Model II regressions between predicted and observed data are given together with the significance of the
688 variance explained by the model. Root mean square error (RMSE), Nash Sutcliffe model efficiency (E) [*Nash and Sutcliffe*, 1970], index of
689 agreement (d) [*Wilmot*, 1981], their modified versions E1 and d1 () and the Cost function (CF) [*OSPAR Commission*, 1998] are shown in the
690 following columns. Quality levels are based on data presented in Table 1.

Simulation		Velocity component	Model II regression			RMSE	E	d	E1	d1	CF
			Slope	Y-intercept	F (explained variance)						
July 2007	Surface layers	u	5.67	0.02	P << 0.001	0.07	**Poor** -4.17	0.49	**Poor** -1.44	0.34	**Good** 1.84
		v	1.99	-0.02	P << 0.001	0.07	**Poor** -0.75	0.62	**Poor** -0.41	0.42	**Good** 1.08
	Intermediate layers	u	1.18	-0.02	P << 0.001	0.05	**Good** 0.27	**0.82**	**Poor** 0.13	0.61	**Very good** 0.68
		v	0.82	0.02	P << 0.001	0.05	**Very good** 0.63	**0.89**	**Good** 0.42	**0.69**	**Very good** 0.47
	Bottom layers	u	0.65	0.01	P << 0.001	0.04	**Excellent** 0.70	**0.89**	**Good** 0.50	**0.71**	**Very good** 0.41
		v	0.56	-0.01	P << 0.001	0.04	**Excellent** 0.69	**0.87**	**Good** 0.49	**0.68**	**Very good** 0.42
	Surface layers	u	2.93	0.12	P << 0.001	0.08	**Poor** -1.56	0.52	**Poor** -0.19	0.51	**Good** 1.01
		v	0.65	-0.01	P << 0.001	0.08	**Poor**	0.48	**Poor**	0.43	**Very**

32

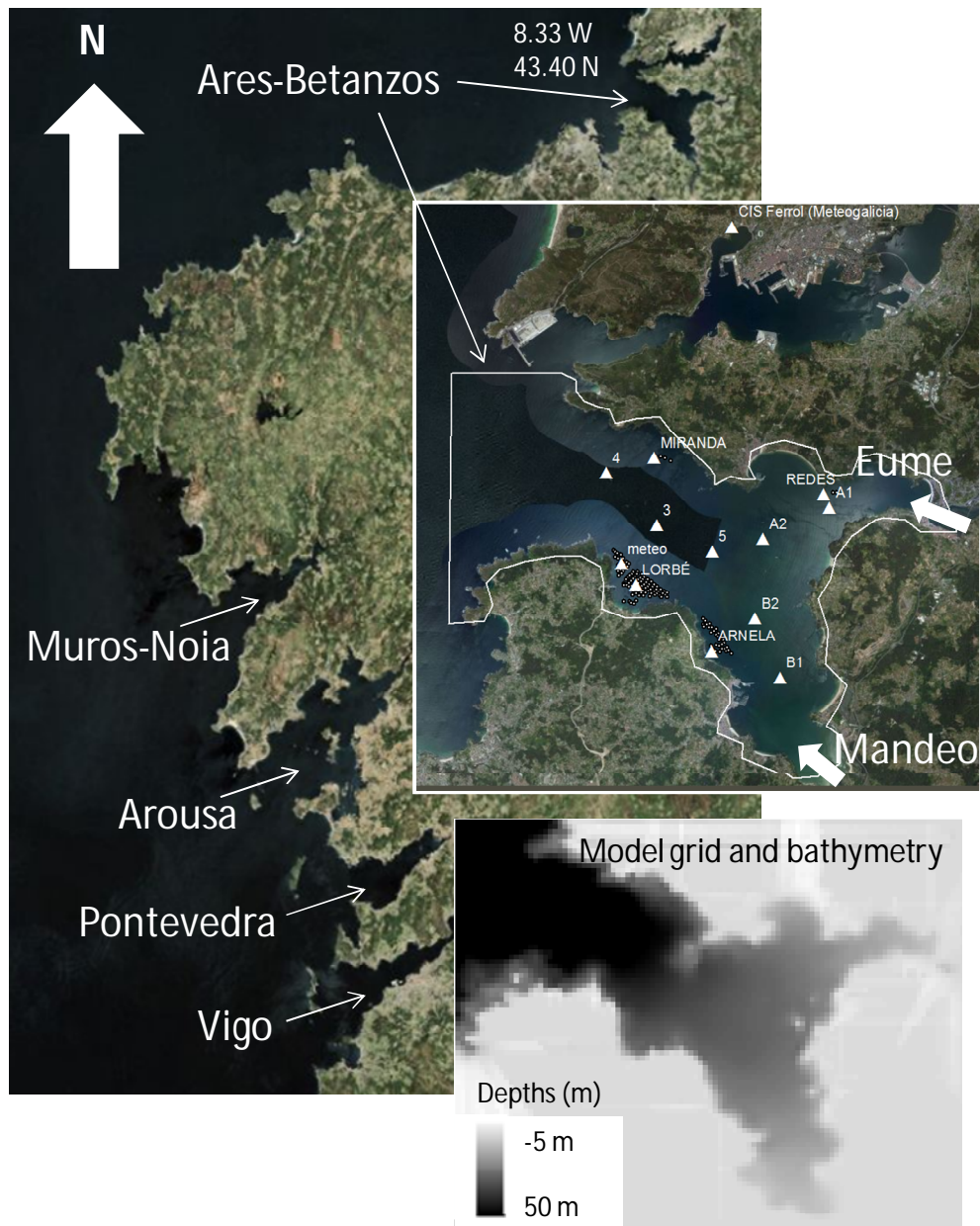| Time	Layer									
				-0.71				-0.13		**good** 0.85
October 2007	Intermediate layers	*u*	1.12	-0.01	P << 0.001	0.05	**Good** 0.34	**0.83**	**Good** 0.20	0.62	**Very good** 0.50
		v	1.41	0.01	P << 0.001	0.03	**Good** 0.28	**0.85**	**Poor** 0.17	0.65	**Very good** 0.54
	Bottom layers	*u*	0.97	0.00	P << 0.001	0.03	**Very good** 0.58	**0.88**	**Good** 0.38	**0.69**	**Very good** 0.41
		v	1.17	0.00	P << 0.001	0.02	**Good** 0.45	**0.87**	**Good** 0.26	0.67	**Very good** 0.47

691 **Figure captions**

692 Figure 1 – Galician ría with a detail of ría de Ares-Betanzos, showing monitoring

693 stations (triangles), the location of mussel rafts (small white dots), model domain

694 (continuous line) and rivers Eume and Mandeo. A raster image with the bathymetry and

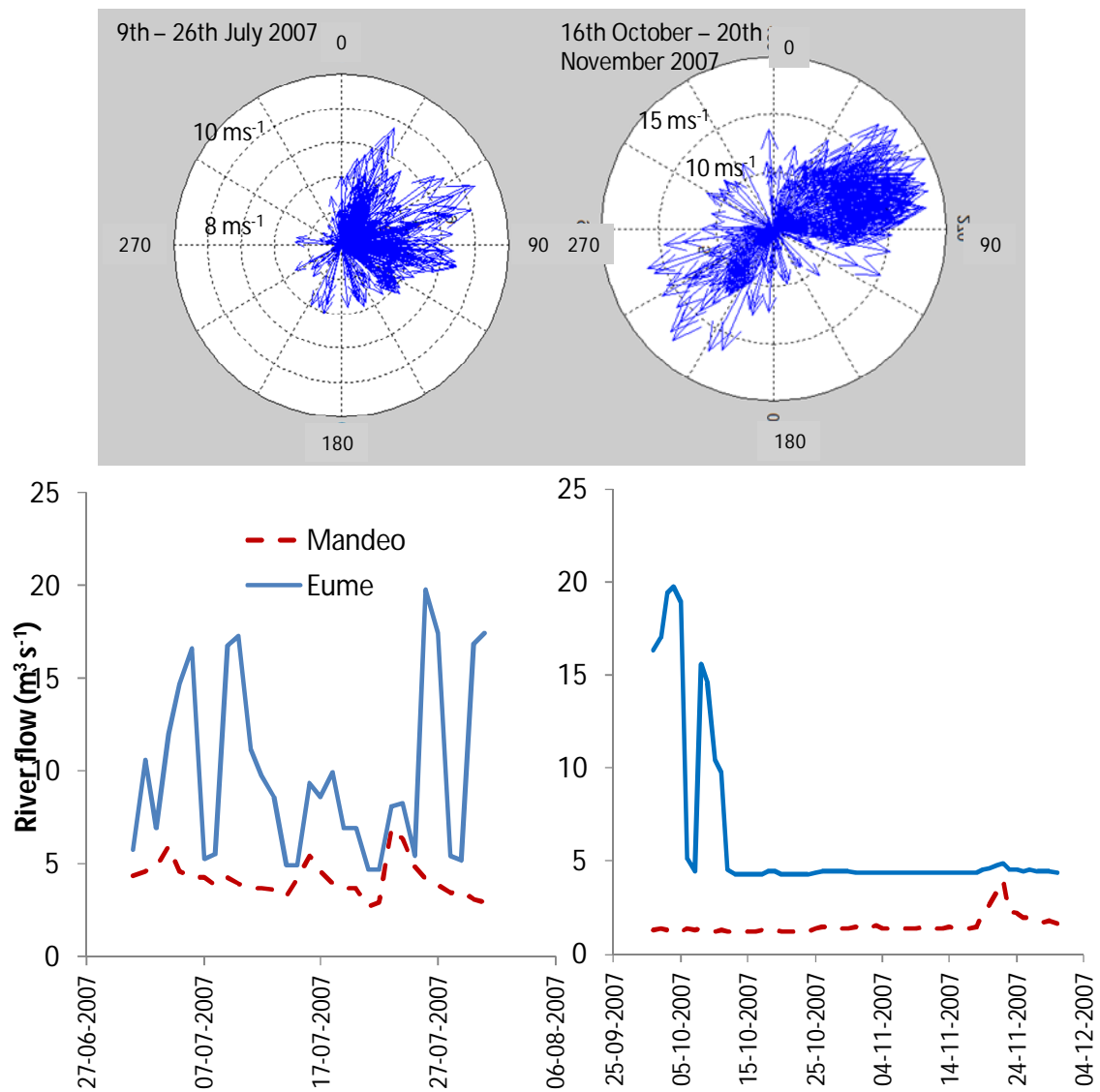695 model grid is also shown (see text).

696 Figure 2 – Wind velocity and direction and river flow data used to force the model for

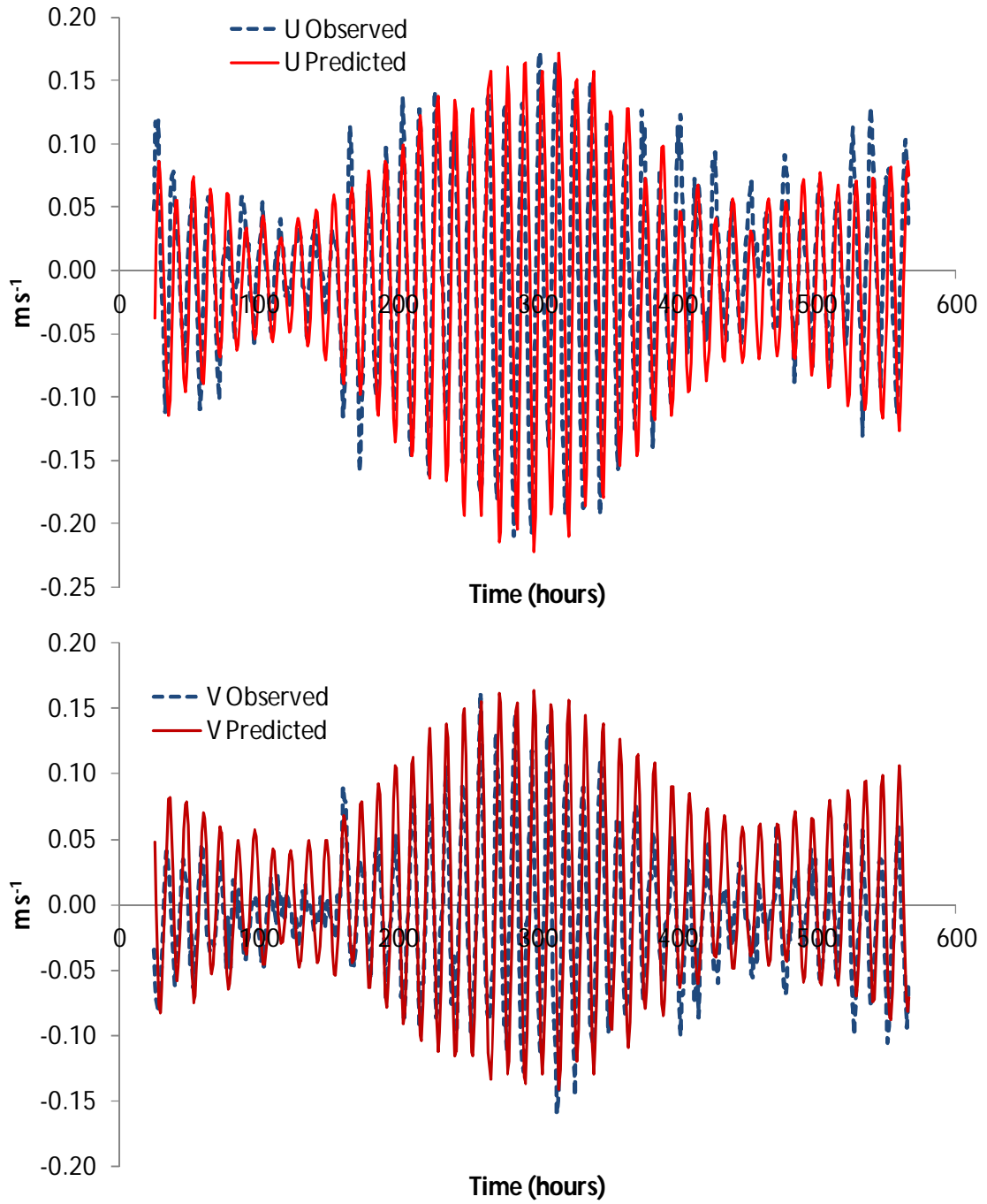697 the periods covered by the simulations (see text).

698 Figure 3 – Predicted and observed u (east-west) and v (north-south) velocity

699 components over a period of 550 h, from October 16th till November 7th 2007 at station

700 3 (cf. Figure 1) between c.a. 6 and 12 m depth.

701 Figure 4 – Predicted and observed vertical profiles of water temperature and salinity in

702 19th July 2007, at several stations depicted in Figure 1 (3, 4, A1 and B1), nine days after

703 simulation started.

704 Figure 5 – Residual velocities predicted by the model for the simulations July – St, July-

705 3 and July-4 (cf. – Table 1) integrated for the upper eight layers (left maps) and for the

706 bottom seven layers (right maps) (see text).

707 Figure 6 – Residual velocities predicted by the model for the simulations October – St,

708 October -3 and October-4 (cf. – Table 1) integrated for the upper eight layers (left maps)

709 and for the bottom seven layers (right maps) (see text).

710 Figure 7 – Predicted daily averaged residual flows (m^3 s^{-1}) for both the July and the

711 October simulations (July-St, July-1, October-St and October-1) (cf. – Table 1), for part

712 of the period covered by the work of *Villegas-Ríos et al.* [2011] and for the boundaries

713 of their box-model. Surface and bottom values were integrated for the upper eight and

714 for the lower seven layers, respectively.

715   Figure 8 – Predicted daily averaged residual flows ($m^3 s^{-1}$) for both the July and the

716   October simulations (July-2, July-3, July-4, October-2, October-3 and October-4) (cf. –

717   Table 1), for the part of the period covered by the work of *Villegas-Ríos et al.* [2011]

718   and for the boundaries of their box-model. Surface and bottom values were integrated

719   for the upper eight and for the lower seven layers, respectively.

720   Figure 9 – Percent differences in residual velocities integrated over time and depth

721   between simulations with and without mussel raft body drag (see text). Upper panel and

722   lower panels: average results integrated for the upper eight layers and the lower seven

723   layers, respectively.

Figure 1 – Galician ría with a detail of ría de Ares-Betanzos, showing monitoring stations (triangles), the location of mussel rafts (small white dots), model domain (continuous line) and rivers Eume and Mandeo. A raster image with the bathymetry and model grid is also shown (see text).

Figure 2 – Wind velocity and direction and river flow data used to force the model for the periods covered by the simulations (see text).

Figure 3 – Predicted and observed u (east-west) and v (north-south) velocity components over a period of 550 h, from October 16th till November 7th 2007 at station 3 (cf. Figure 1) between c.a. 6 and 12 m depth.
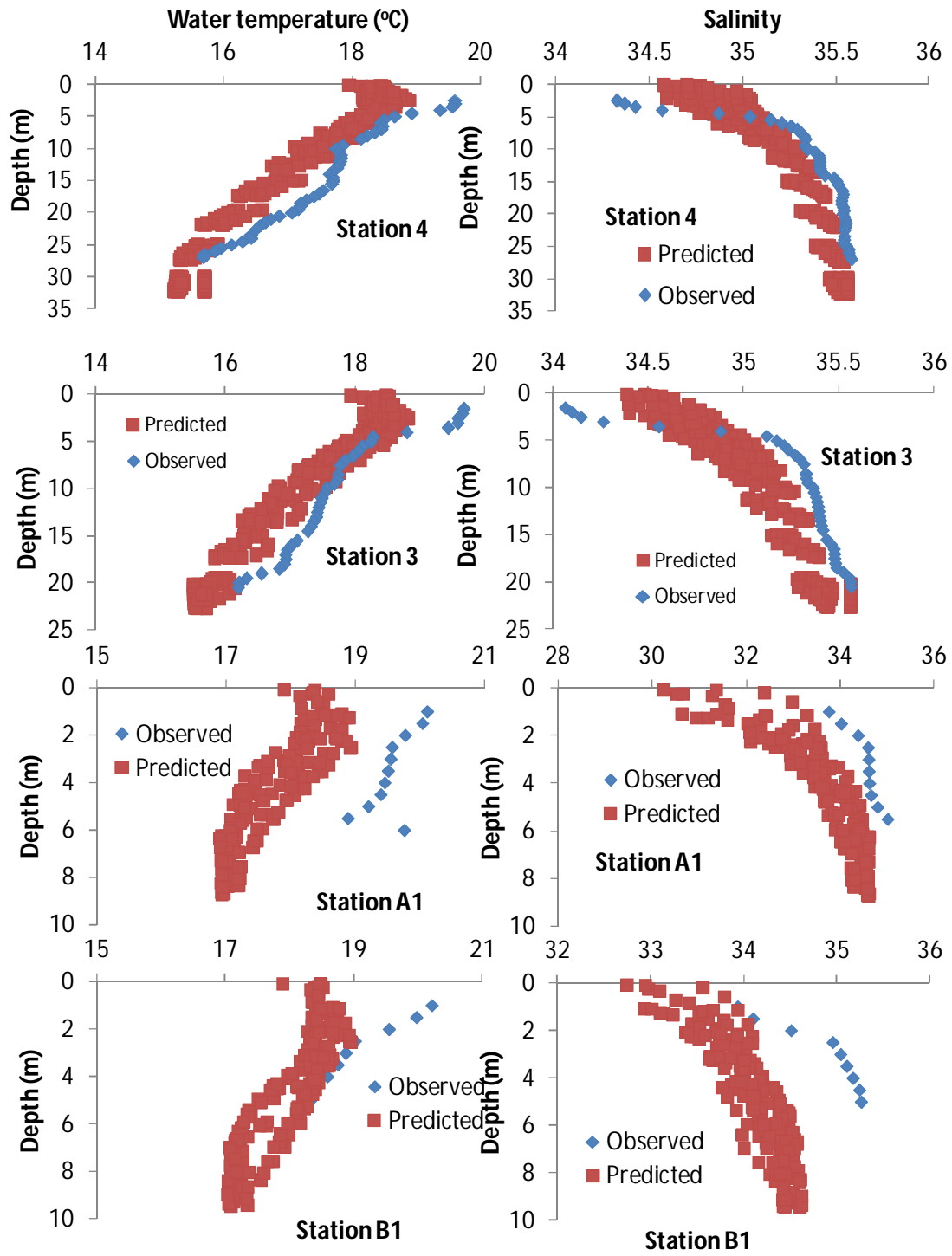
Figure 4 – Predicted and observed vertical profiles of water temperature and salinity in 19th July 2007, at several stations depicted in Figure 1 (3, 4, A1 and B1), nine days after simulation started.
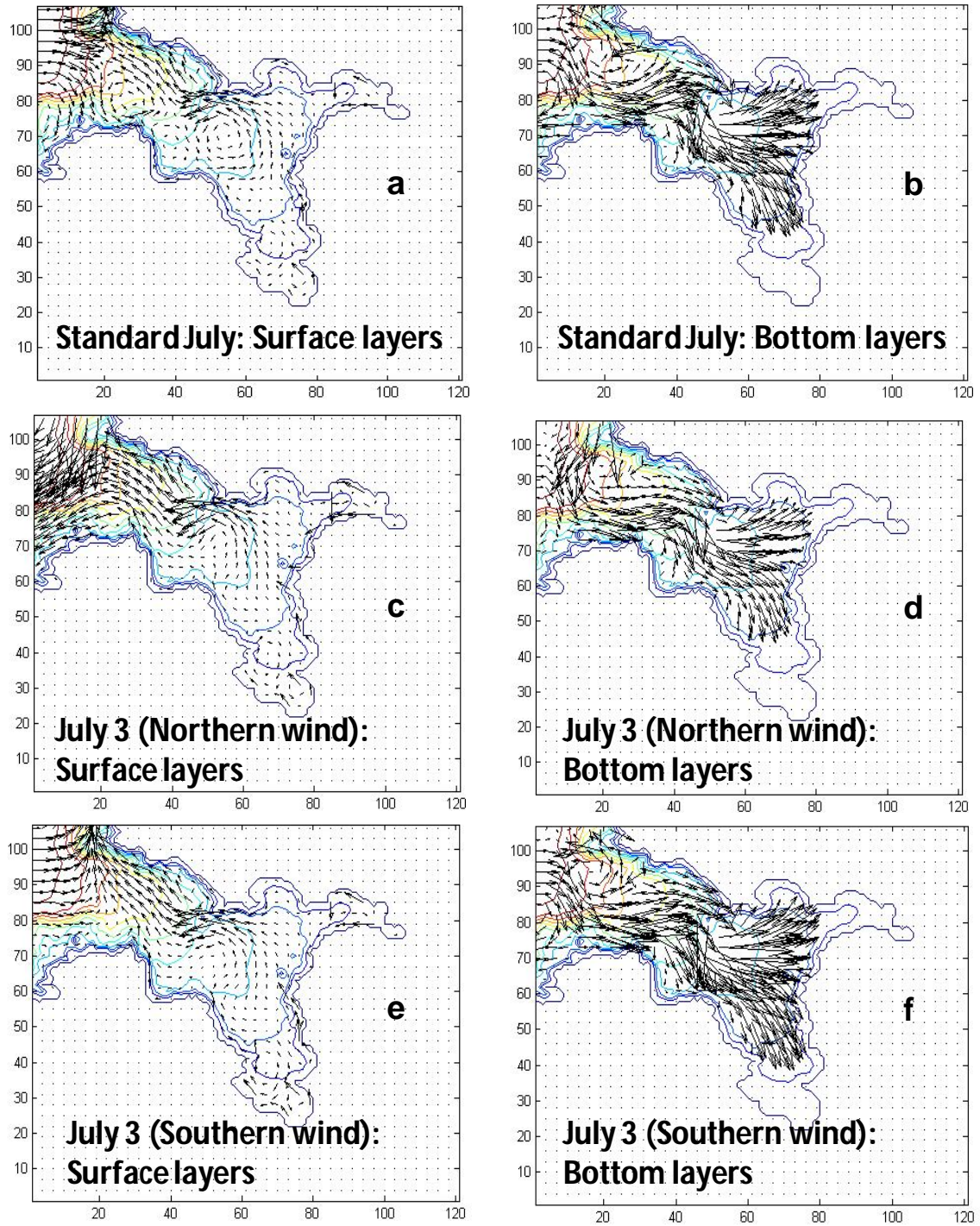
Figure 5 – Residual velocities predicted by the model for the simulations July – St, July-3 and July-4 (cf. – Table 1) integrated for the upper eight layers (left maps) and for the bottom seven layers (right maps) (see text).
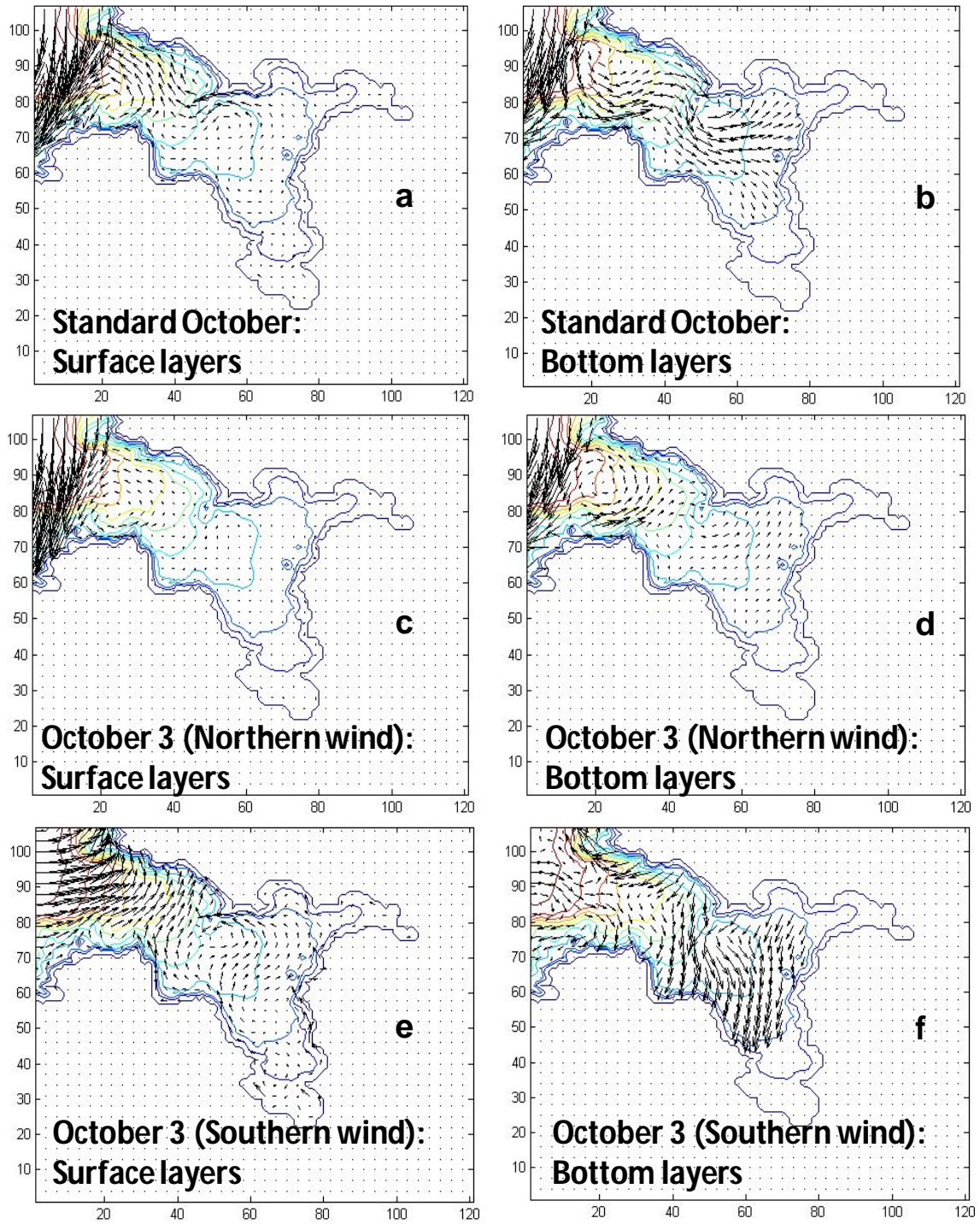
Figure 6 – Residual velocities predicted by the model for the simulations October – St, October -3 and October-4 (cf. – Table 1) integrated for the upper eight layers (left maps) and for the bottom seven layers (right maps) (see text).
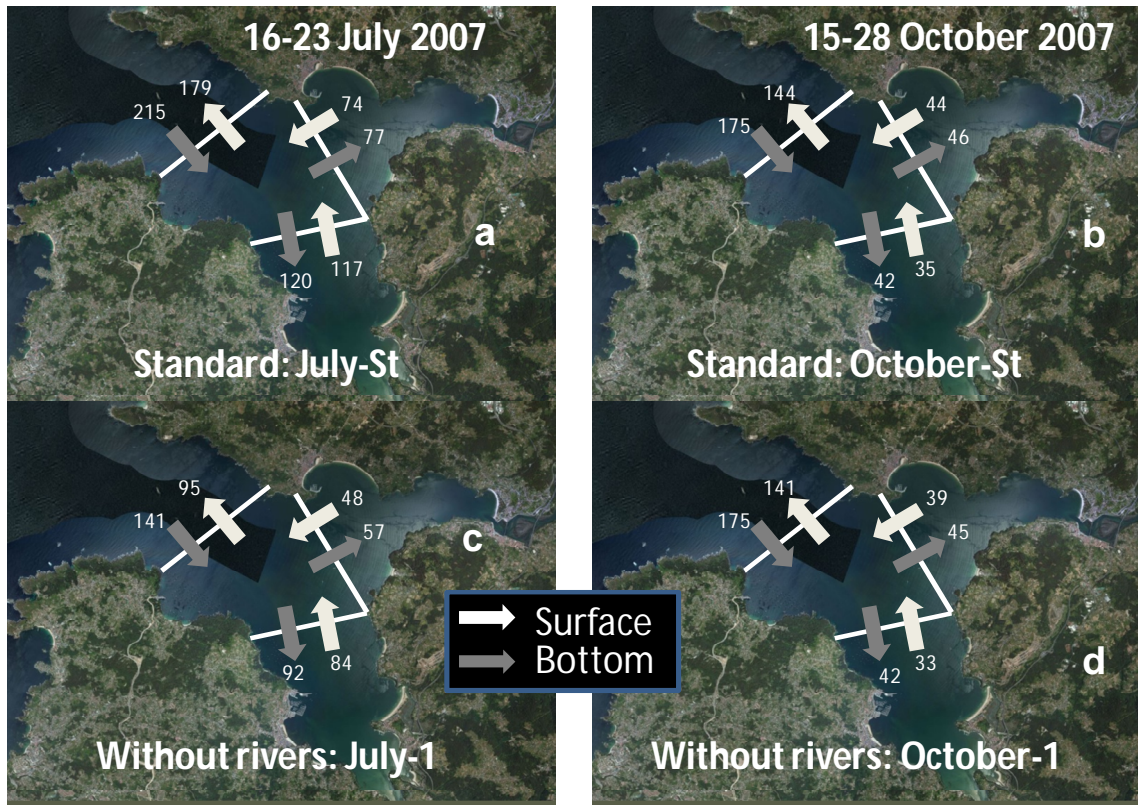
Figure 7 – Predicted daily averaged residual flows (m^3 s^{-1}) for both the July and the October simulations (July-St, July-1, October-St and October-1) (cf. – Table 1), for part of the period covered by the work of *Villegas-Ríos et al*. [2011] and for the boundaries of their box-model. Surface and bottom values were integrated for the upper eight and for the lower seven layers, respectively.
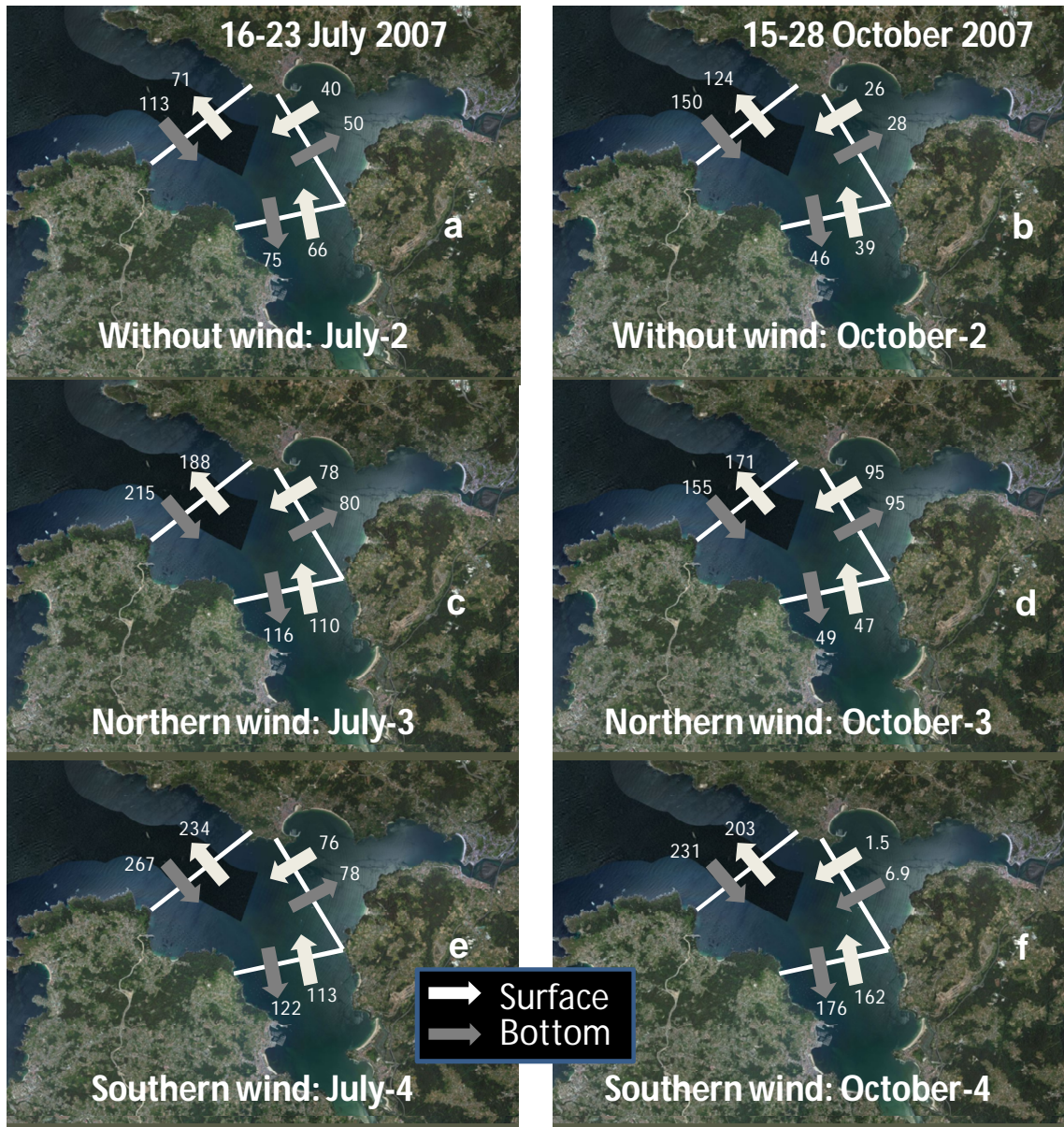
Figure 8 – Predicted daily averaged residual flows (m^3 s^{-1}) for both the July and the October simulations (July-2, July-3, July-4, October-2, October-3 and October-4) (cf. – Table 1), for the part of the period covered by the work of *Villegas-Ríos et al.* [2011] and for the boundaries of their box-model. Surface and bottom values were integrated for the upper eight and for the lower seven layers, respectively.
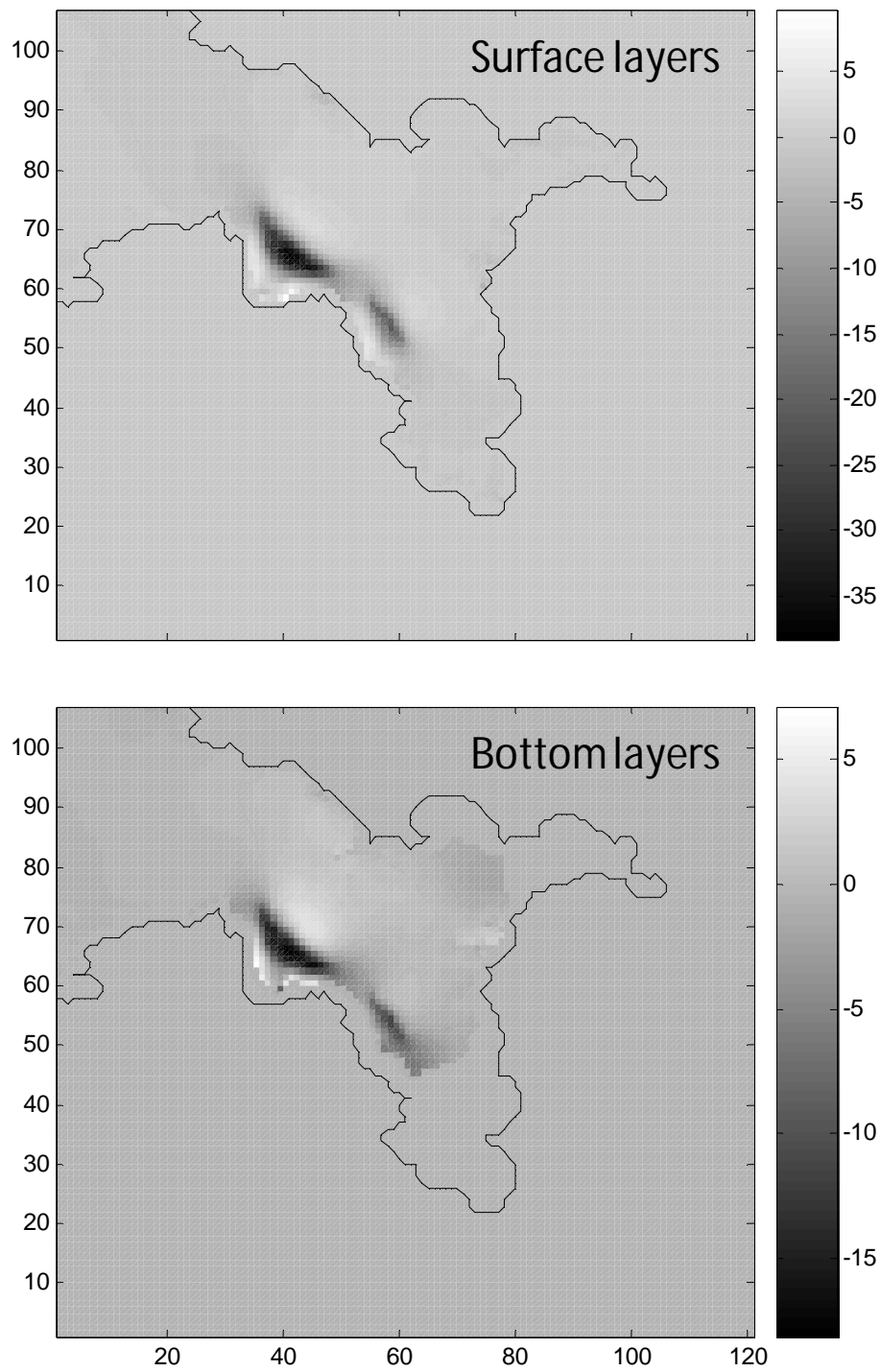
Figure 9 – Percent differences in residual velocities integrated over time and depth between simulations with and without mussel raft body drag (see text). Upper panel and lower panels: average results integrated for the upper eight layers and the lower seven layers, respectively.